

Conformal confidence sets for biomedical image segmentation

Samuel Davenport

October 2, 2024

Abstract

We develop confidence sets which provide spatial uncertainty guarantees for the output of a black-box machine learning model designed for image segmentation. To do so we adapt conformal inference to the imaging setting, obtaining thresholds on a calibration dataset based on the distribution of the maximum of the transformed logit scores within and outside of the ground truth masks. We prove that these confidence sets, when applied to new predictions of the model, are guaranteed to contain the true unknown segmented mask with desired probability. We show that learning appropriate score transformations on a learning dataset before performing calibration is crucial for optimizing performance. We illustrate and validate our approach on a polyps tumor dataset. To do so we obtain the logit scores from a deep neural network trained for polyps segmentation and show that using distance transformed scores to obtain outer confidence sets and the original scores for inner confidence sets enables tight bounds on tumor location whilst controlling the false coverage rate.

1 Introduction

Deep neural networks promise to significantly enhance a wide range of important tasks in biomedical imaging. However these models, as typically used, lack formal uncertainty guarantees on their output which can lead to overconfident predictions and critical errors (Guo et al., 2017; Gupta et al., 2020). Misclassifications or inaccurate segmentations can lead to serious consequences, including misdiagnosis, inappropriate treatment decisions, or missed opportunities for early intervention (Topol, 2019). Without uncertainty quantification, medical professionals cannot rely on deep learning models to provide accurate information and predictions which can limit their use in practical applications (Jungo et al., 2020).

In order to address this problem, conformal inference, a robust framework for uncertainty quantification, has become increasingly used as a means of providing prediction guarantees, offering reliable, distribution-free confidence sets for the output of neural networks which have finite sample validity. This approach, originally introduced in Papadopoulos et al. (2002); Vovk et al. (2005), has become increasingly popular due to its ability to provide rigorous statistical guarantees without making strong assumptions about the underlying data distribution or model architecture. Conformal prediction methods, in their most commonly used form - split conformal inference - work by calibrating the predictions of the model on a held-out dataset in order to provide sets which

contain the output with a given probability, see Shafer and Vovk (2008) and Angelopoulos and Bates (2021) for good introductions.

In the context of image segmentation, we have a decision to make at each pixel/voxel of an image which can lead to a large multiple testing problem. Traditional conformal methods, typically designed for scalar outputs, require adaptation to handle multiple tests and their inherent spatial dependencies. To do so Angelopoulos et al. (2021) applied conformal inference pixelwise and performed multiple testing correction on the resulting p -values, however this approach does not account for the complex dependence structure inherent in the images. To take advantage of this structure, in an approach analogous to the FDR control of (Benjamini and Hochberg, 1995), Bates et al. (2021) and Angelopoulos et al. (2024) sought to control the expected risk of a given loss function over the image and used a conformal approach to produce outer confidence sets for segmented images which control the expected proportion of false negatives. Other work considering conformal inference in the context of multiple dependent hypotheses includes Marandon (2024) and Blanchard et al. (2024) who established conformal FDR control when testing for the presence of missing links in graphs.

In this work we argue that bounding the segmented outcome with guarantees in probability rather than on the proportion of discoveries is more informative, avoiding errors at the borders of potential tumors. This is analogous to the tradeoff between FWER and FDR/FDP control in the multiple testing literature in which there is a balance between power and coverage rate, the distinction being that in medical image segmentation making mistakes can have potentially serious consequences. Under-segmentation might cause part of the tumor to be missed, potentially leading to inadequate treatment (Jalalifar et al., 2022). Over-segmentation, on the other hand, could result in unnecessary interventions, increasing patient risk and healthcare costs (Gupta et al., 2020; Patz et al., 2014). Confidence sets are instead guaranteed to contain the outcome with a given level of certainty. Since the guarantees are more meaningful the problem is more difficult and existing work on conformal uncertainty quantification for images has thus often focused on producing sets with guarantees on the proportions of discoveries or pixel level inference rather than coverage (Bates et al. (2021), Wieslander et al. (2020), Mossina et al. (2024)) which is a stricter error criterion.

In order to obtain confidence sets we use a split-conformal inference approach in which we learn appropriate cutoffs, with which to threshold the output of an image segmenter, from a calibration dataset. These thresholds are obtained by considering the distribution of the maximum logit (transformed) scores provided by the model within and outside of the ground truth masks. This approach allows us to capture the spatial nature of the uncertainty in segmentation tasks, going beyond simple pixel-wise confidence measures. By applying these learned thresholds to new predictions, we can generate inner and outer confidence sets that are guaranteed to contain the true, unknown segmented mask with a desired probability. As we shall see, naively using the original model scores to do so can lead to rather large and uninformative outer confidence sets but these can be greatly improved using distance transformations.

2 Theory

2.1 Set up

Let $\mathcal{V} \subset \mathbb{R}^m$, for some dimension $m \in \mathbb{N}$, be a finite set corresponding to the domain which represents the pixels/voxels/points at which we observe imaging data. Let $\mathcal{X} = \{g : \mathcal{V} \rightarrow \mathbb{R}\}$ be the set of real functions on \mathcal{V} and let $\mathcal{Y} = \{g : \mathcal{V} \rightarrow \{0, 1\}\}$ be the set of all functions on \mathcal{V} taking the values 0 or 1. We shall refer to elements of \mathcal{X} and \mathcal{Y} as images. Suppose that we observe a calibration dataset $(X_i, Y_i)_{i=1}^n$ of random images, where $X_i : \mathcal{V} \rightarrow \mathbb{R}$ represents the i th observed calibration image and $Y_i : \mathcal{V} \rightarrow \{0, 1\}$ outputs labels at each $v \in \mathcal{V}$ giving 1s at the true location of the objects in the image X_i that we wish to identify and 0s elsewhere. Let $\mathcal{P}(\mathcal{V})$ be the set of all subsets of \mathcal{V} . Given a function $f : \mathcal{X} \rightarrow \mathcal{X}$, we shall write $f(X, v)$ to denote $f(X)(v)$ for all $v \in \mathcal{V}$.

Let $s : \mathcal{X} \rightarrow \mathcal{X}$ be a score function - trained on an independent dataset - such that given an image pair $(X, Y) \in \mathcal{X} \times \mathcal{Y}$, $s(X)$ is a score image in which $s(X, v)$ is intended to be higher at the $v \in \mathcal{V}$ for which $Y(v) = 1$. The score function can for instance be the logit scores obtained from applying a deep neural network image segmentation method to the image X . Given $X \in \mathcal{X}$, let $\hat{M}(X) \in \mathcal{Y}$ be the predicted mask given by the model which is assumed to be obtained using the scores $s(X)$.

In what follows we will use the calibration dataset to construct confidence functions $I, O : \mathcal{X} \rightarrow \mathcal{P}(\mathcal{V})$ such that for a new image pair (X, Y) , given error rates $\alpha_1, \alpha_2 \in (0, 1)$ we have

$$\mathbb{P}(I(X) \subseteq \{v \in \mathcal{V} : Y(v) = 1\}) \geq 1 - \alpha_1, \quad (1)$$

$$\text{and } \mathbb{P}(\{v \in \mathcal{V} : Y(v) = 1\} \subseteq O(X)) \geq 1 - \alpha_2. \quad (2)$$

Here $I(X)$ and $O(X)$ serve as inner and outer confidence sets for the location of the true segmented mask. Their interpretation is that, up to the guarantees provided by the probabilistic statements (1) and (2), we can be sure that for each $v \in I(X)$, $Y(v) = 1$ or that for each $v \notin O(X)$, $Y(v) = 0$. Joint control over the events can also be guaranteed, either via sensible choices of α_1 and α_2 or by using the joint distribution of the maxima of the logit scores - see Section 2.3.

In order to establish conformal confidence results we shall require the following exchangeability assumption.

Assumption 1. Given a new random image pair, (X_{n+1}, Y_{n+1}) , suppose that $(X_i, Y_i)_{i=1}^{n+1}$ is an exchangeable sequence of random image pairs in the sense that

$$\{(X_1, Y_1), \dots, (X_{n+1}, Y_{n+1})\} =_d \{(X_{\sigma(1)}, Y_{\sigma(1)}), \dots, (X_{\sigma(n+1)}, Y_{\sigma(n+1)})\}$$

for all permutations $\sigma \in S_{n+1}$. Here $=_d$ denotes equality in distribution and S_{n+1} is the group of permutations of the integers $\{1, \dots, n+1\}$.

Exchangeability or a variant is a standard assumption in the conformal inference literature (Angelopoulos and Bates, 2021) and facilitates coverage guarantees. It holds for instance if we assume that the collection $(X_i, Y_i)_{i=1}^{n+1}$ is an i.i.d. sequence of image pairs but is more general and in principle allows for other dependence structures.

2.2 Marginal confidence sets

In order to construct conformal confidence sets let $f_I, f_O : \mathcal{X} \rightarrow \mathcal{X}$ be inner and outer transformation functions and for each $1 \leq i \leq n+1$, let $\tau_i = \max_{v \in \mathcal{V}: Y_i(v)=0} f_I(s(X_i), v)$

and $\gamma_i = \max_{v \in \mathcal{V}: Y_i(v)=1} -f_O(s(X_i), v)$ be the maxima of the function transformed scores over the areas at which the true labels equal 0 and 1 respectively. We will require the following assumption on the scores and the transformation functions.

Assumption 2. (Independence of scores) $(X_i, Y_i)_{i=1}^{n+1}$ is independent of the functions s, f_O, f_I .

Given this we construct confidence sets as follows.

Theorem 2.1. (*Marginal inner set*) Under Assumptions 1 and 2, given $\alpha_1 \in (0, 1)$, let

$$\lambda_I(\alpha_1) = \inf \left\{ \lambda : \frac{1}{n} \sum_{i=1}^n 1[\tau_i \leq \lambda] \geq \frac{\lceil (1-\alpha_1)(n+1) \rceil}{n} \right\},$$

and define $I(X) = \{v \in \mathcal{V} : f_I(s(X), v) > \lambda_I(\alpha_1)\}$. Then,

$$\mathbb{P}(I(X_{n+1}) \subseteq \{v \in \mathcal{V} : Y_{n+1}(v) = 1\}) \geq 1 - \alpha_1. \quad (3)$$

Proof. Under Assumptions 1 and 2, exchangeability of the image pairs implies exchangeability of the sequence $(\tau_i)_{i=1}^{n+1}$. In particular, $\lambda_I(\alpha_1)$ is the upper α_1 quantile of the distribution of $(\tau_i)_{i=1}^n \cup \{\infty\}$ and so, by Lemma 1 of Tibshirani et al. (2019), it follows that

$$\mathbb{P}(\tau_{n+1} \leq \lambda_I(\alpha_1)) \geq 1 - \alpha_1.$$

Now consider the event that $\tau_{n+1} \leq \lambda_I(\alpha_1)$. On this event, $f_I(s(X_{n+1}), v) \leq \lambda_I(\alpha_1)$ for all $v \in \mathcal{V}$ such that $Y_{n+1}(v) = 0$. As such, given $u \in \mathcal{V}$ such that $f_I(s(X_{n+1}), u) > \lambda_I(\alpha_1)$, we must have $Y_{n+1}(u) = 1$ and so $I(X_{n+1}) \subseteq \{v \in \mathcal{V} : Y_{n+1}(v) = 1\}$. It thus follows that

$$\mathbb{P}(I(X_{n+1}) \subseteq \{v \in \mathcal{V} : Y_{n+1}(v) = 1\}) \geq \mathbb{P}(\tau_{n+1} \leq \lambda_I(\alpha_1)) \geq 1 - \alpha_1.$$

□

For the outer set we have the following analogous result.

Theorem 2.2. (*Marginal outer set*) Under Assumptions 1 and 2, given $\alpha_2 \in (0, 1)$, let

$$\lambda_O(\alpha_2) = \inf \left\{ \lambda : \frac{1}{n} \sum_{i=1}^n 1[\gamma_i \leq \lambda] \geq \frac{\lceil (1-\alpha_2)(n+1) \rceil}{n} \right\},$$

and define $O(X) = \{v \in \mathcal{V} : -f_O(s(X), v) \leq \lambda_O(\alpha_2)\}$. Then,

$$\mathbb{P}(\{v \in \mathcal{V} : Y_{n+1}(v) = 1\} \subseteq O(X_{n+1})) \geq 1 - \alpha_2. \quad (4)$$

Proof. Arguing as in the proof of Theorem 2.1, it follows that $\mathbb{P}(\gamma_{n+1} \leq \lambda_O(\alpha_2)) \geq 1 - \alpha_2$. Now on the event that $\gamma_{n+1} \leq \lambda_O(\alpha_2)$ we have $-f_O(s(X_{n+1}), v) \leq \lambda_O(\alpha_2)$ for all $v \in \mathcal{V}$ such that $Y_{n+1}(v) = 1$. As such, given $u \in \mathcal{V}$ such that $-f_O(s(X_{n+1}), u) > \lambda_O(\alpha_2)$, we must have $Y_{n+1}(u) = 0$ and so $O(X)^C \subseteq \{v \in \mathcal{V} : Y_{n+1}(v) = 0\}$. The result then follows as above. □

Remark 2.3. We have used the maximum over the transformed scores in order to combine score information on and off the ground truth masks. The maximum is a natural combination function in imaging and is commonly used in the context of multiple testing (Worsley et al., 1992). However the theory above is valid for any increasing combination function. We show this in Appendix A.1 where we establish generalized versions of these results.

Remark 2.4. Inner and outer coverage can also be viewed as a special case of conformal risk control with an appropriate choice of loss function. We can thus instead establish coverage results as a corollary to risk control, see Appendix A.2 for details. This amounts to an alternative proof of the results as the proof of the validity of risk control is different though still strongly relies on exchangeability.

2.3 Joint confidence sets

Instead of focusing on marginal control one can instead spend all of the α available to construct sets which have a joint probabilistic guarantees. This gain comes at the expense of a loss of precision. The simplest means of constructing jointly valid confidence sets is via the marginal sets themselves.

Corollary 2.5. (*Joint from marginal*) Assume Assumptions 1 and 2 hold and given $\alpha \in (0, 1)$ and $\alpha_1, \alpha_2 \in (0, 1)$ such that $\alpha_1 + \alpha_2 \leq \alpha$, define $I(X)$ and $O(X)$ as in Theorems 2.1 and 2.2. Then

$$\mathbb{P}(I(X_{n+1}) \subseteq \{v \in \mathcal{V} : Y_{n+1}(v) = 1\} \subseteq O(X_{n+1})) \geq 1 - \alpha. \quad (5)$$

Alternatively joint control can be obtained using the joint distribution of the maxima of the transformed logit scores as follows.

Theorem 2.6. (*Joint coverage*) Assume that Assumption 1 and 2 hold. Given $\alpha \in (0, 1)$, define

$$\lambda(\alpha) = \inf \left\{ \lambda : \frac{1}{n} \sum_{i=1}^n \mathbf{1}[\max(\tau_i, \gamma_i) \leq \lambda] \geq \frac{\lceil (1 - \alpha)(n + 1) \rceil}{n} \right\}.$$

Let $O(X) = \{v \in \mathcal{V} : -f_O(s(X), v) \leq \lambda(\alpha)\}$ and $I(X) = \{v \in \mathcal{V} : f_I(s(X), v) > \lambda(\alpha)\}$. Then,

$$\mathbb{P}(I(X_{n+1}) \subseteq \{v \in \mathcal{V} : Y_{n+1}(v) = 1\} \subseteq O(X_{n+1})) \geq 1 - \alpha. \quad (6)$$

Proof. Exchangeability of the image pairs implies exchangeability of the sequence $(\tau_i, \gamma_i)_{i=1}^{n+1}$. Moreover on the event that $\max(\tau_{n+1}, \gamma_{n+1}) \leq \lambda(\alpha)$ we have $\tau_{n+1} \leq \lambda(\alpha)$ and $\gamma_{n+1} \leq \lambda(\alpha)$ so the result follows via a proof similar to that of Theorems 2.1 and 2.2. \square

Remark 2.7. The advantage of Corollary 2.5 is that the resulting inner and outer sets provide pivotal inference - not favouring one side or the other - which can be important when the distribution of the score function is asymmetric. Moreover the levels α_1 and α_2 can be used to provide a greater weight to either inner or outer sets whilst maintaining joint coverage. Theorem 2.6 may instead be useful when there is strong dependence between τ_{n+1} and γ_{n+1} . However, when this dependence is weak, scale differences in the scores can lead to a lack of pivotality. This can be improved by appropriate choices of the score transformations f_I and f_O however in practice it may be simpler to construct joint sets using Corollary 2.5.

2.4 Optimizing score transformations

The choice of score transformations f_I and f_O is extremely important and can have a large impact on the size of the conformal confidence sets. The best choice depends on both the distribution of the data and on the nature of the output of the image segmentor used to calculate the scores. We thus recommend setting aside a learning dataset independent

from both the calibration dataset, used to compute the conformal thresholds, and the test dataset. This approach was used in Sun and Yu (2024) to learn the best copula transformation for combining dependent data streams.

In order to make efficient use of the data available, the learning dataset can in fact contain some or all of the data used to train the image segmentor. This data is assumed to be independent of the calibration and test data and so can be used to learn the best score transformations without compromising subsequent validity. The advantage of doing so is that less additional data needs to be set aside or collected for the purposes of learning a score function. Moreover it allows for additional data to be used to train the model resulting in better segmentation performance. The disadvantage is that machine learning models typically overfit their training data meaning that certain score functions may appear to perform better on this data than they do in practice. The choice of whether to include training data in the learning dataset thus depends on the quantity of data available and the quality of the segmentation model.

A score transformation that we will make particular use of in Section 3 is based on the distance transformation which we define as follows. Given $\mathcal{A} \subseteq \mathcal{V}$, let $E(\mathcal{A})$ be the set of points on the boundary of \mathcal{A} obtained using the marching squares algorithm (Maple, 2003). Given a distance metric ρ define the distance transformation $d_\rho : \mathcal{P}(\mathcal{V}) \times \mathcal{V} \rightarrow \mathbb{R}$, which sends $\mathcal{A} \in \mathcal{P}(\mathcal{V})$ and $v \in \mathcal{V}$ to

$$d_\rho(\mathcal{A}, v) = \text{sign}(\mathcal{A}, v) \min\{\rho(v, e) : e \in E(\mathcal{A})\},$$

where $\text{sign}(\mathcal{A}, v) = 1$ if $v \in \mathcal{A}$ and equals -1 otherwise. The function d_ρ is an adaption of the distance transform of Borgefors (1986) which provides positive values within the set \mathcal{A} and negative values outside of \mathcal{A} .

2.5 Constructing confidence sets from bounding boxes

Existing work on conformal inner and outer confidence sets, which aim to provide coverage of the entire ground truth mask with a given probability, has primarily focused on bounding boxes (de Grancey et al., 2022; Andéol et al., 2023; Mukama et al., 2024). These papers adjust for multiple comparisons over the 4 edges of the bounding box, doing so conformally by comparing the distance between the predicted bounding box and the bounding box of the ground truth mask. These approaches aggregate the predictions over all objects within all of the calibration images, often combining multiple bounding boxes per image. However, as observed in Section 5 of de Grancey et al. (2022), doing so violates exchangeability which is needed for valid conformal inference, as there is dependence between the objects within each image. These papers do not provide formal proofs and their theoretical validity is thus unclear.

In order to provide a more formal justification of bounding box methods we establish the validity of an adapted version of the max-additive method of Andéol et al. (2023) as a corollary to our results, see Appendix A.3. In this approach we define bounding box scores based on the chessboard distance transformation to the inner and outer predicted masks and use these scores to provide conformal confidence sets. Validity then follows as a consequence of the results above as we show in Corollaries A.5 and A.6. We compare to this approach in our experiments below. Targeting bounding boxes does not directly target the mask itself and so the resulting confidence sets are typically conservative.

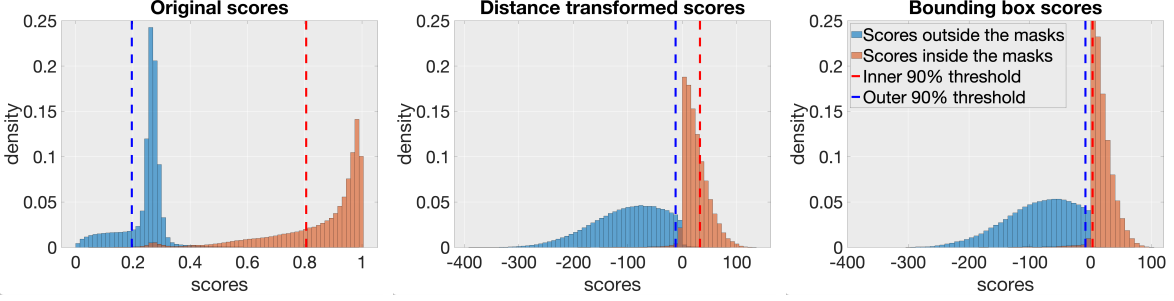


Figure 1: Histograms of the distribution of the scores over the whole image within and outside the ground truth masks. Thresholds obtained for the marginal 90% inner and outer confidence sets, obtained based on quantiles of the distribution of $(\tau_i)_{i=1}^n$ and $(\gamma_i)_{i=1}^n$, are displayed in red and blue.

3 Application to Polyps tumor segmentation

In order to illustrate and validate our approach we consider the problem of polyps tumor segmentation. To do so we use the same dataset as in Angelopoulos et al. (2024) in which 1798 polyps images, with available ground truth masks were combined from 5 open-source datasets (Pogorelov et al. (2017), Borgli et al. (2020) Bernal et al. (2012), Silva et al. (2014)). Logit scores were obtained for these images using the parallel reverse attention network (PraNet) model (Fan et al., 2020).

3.1 Choosing a score transformation

In order to optimize the size of our confidence sets we set aside 298 of the 1798 polyps images to form a learning dataset on which to choose the best score transformations. Importantly as the learning dataset is independent of the remaining 1500 images set-aside, we can study it as much as we like without compromising the validity of the follow-up analyses in Sections 3.2. In particular in this section we shall use the learning dataset to both calibrate and study the results, in order to maximize the amount of important information we can learn from it.

The score transformations we considered were the identity (after softmax transformation) and distance transformations of the predicted masks: taking $f_I(s(X), v) = f_O(s(X), v) = d_\rho(\hat{M}(X), v)$, where ρ is the Euclidean metric. We also compare to the results of using the bounding box transformations $f_I = b_I$ and $f_O = b_O$ which correspond to transforming the predicted bounding box using a distance transformation based on the chessboard metric and are defined formally in Appendix A.3. For the purposes of plotting we used the combined bounding box scores defined in Definition A.4.

From the histograms in Figure 1 we can see that thresholding the original scores at the inner threshold well separates the data. However this is not the case for the outer threshold for which the data is better separated using the distance transformed and bounding box scores. Figure 2 shows PraNet scores for 2 typical examples, along with surface plots of the transformed scores and corresponding 90% marginal confidence regions (with thresholds obtained from calibrating over the learning dataset). From these we see that PraNet typically assigns a high softmax score to the polyps regions which decreases in the regions directly around the boundary of the tumor before returning to a higher level away from the polyps. This results in tight inner sets but large outer sets as the model struggles to identify where the tumor ends. Instead the distance transformed

and bounding box scores are much better at providing outer bounds on the tumor, with distance transformed scores providing a tighter outside fit. Additional examples are shown in Figures A7 and A8 and have the same conclusion.

Based on the results of the learning dataset we decided to combine the best of the approaches for the inner and outer sets respectively for the inference in Section 3.2, taking f_I to be the identity and f_O to be the distance transformation of the predicted mask in order to optimize performance. We can also use the learning dataset to determine how to weight the α used to obtain joint confidence sets. A ratio of 4 to 1 seems appropriate here in light of the fact that in this dataset identifying where a given tumor ends appears to be more challenging than identifying pixels where we are sure that there is a tumor. To achieve joint coverage of 90% this involves taking $\alpha_1 = 0.02$ and $\alpha_2 = 0.08$.

3.2 Illustrating the performance of conformal confidence sets

In order to illustrate the full extent of our methods in practice we divide the set aside 1500 images at random into 1000 for conformal calibration, and 500 for testing. The resulting conformal confidence sets for 10 example images from the test dataset are shown in Figure 3, with inner sets obtained using the original scores and outer sets using the distance transformed scores. The inner sets are shown in red and represent regions where we can have high confidence of the presence of polyps. The outer sets are shown in blue and represent regions in which the polyps may be. The ground truth mask for each polyp is shown in yellow and can be compared to the original images. In each of the examples considered the ground truth is bounded from within by the inner set and from without by the outer set. Results for confidence sets based on the original and bounding box scores as well as additional examples are available in Figures A9 and A10. Confidence sets can also be provided for the bounding boxes themselves if that is the object of interest, see Figure A11. Joint 90% confidence sets are displayed in Figure A12, from which we can see that with alpha-weighting (i.e. taking $\alpha_1 = 0.02$ and $\alpha_2 = 0.08$) we are able to obtain joint confidence sets which are still relatively tight.

These results collectively show that we can provide informative confidence bounds for the location of the polyps and allow us to use the PraNet segmentation model with uncertainty guarantees. From Figure 3 we can see that the method, which combines the original and the transformed scores, effectively delineates polyps regions. These results also help to make us aware of the limitations of the model, allowing medical practitioners to follow up on outer sets which do not contain inner sets in order to determine whether a tumor is present. Improved uncertainty quantification would require an improved segmentation model.

More precise results can be obtained at the expense of probabilistic guarantees, see Figures A13 and A14. A trade off must be made between precision and confidence. The most informative confidence level can be determined in advance based on the learning dataset and the desired type of coverage.

3.3 Measuring the coverage rate

In this section we run validations to evaluate the false coverage rate of our approach. To do so we take the set aside 1500 images and run 1000 validations, in each validation dividing the data into 1000 calibration and 500 test images. In each division we calculate the conformal confidence sets using the different score transformations, based on thresholds derived from the calibration dataset, and evaluate the coverage rate on the

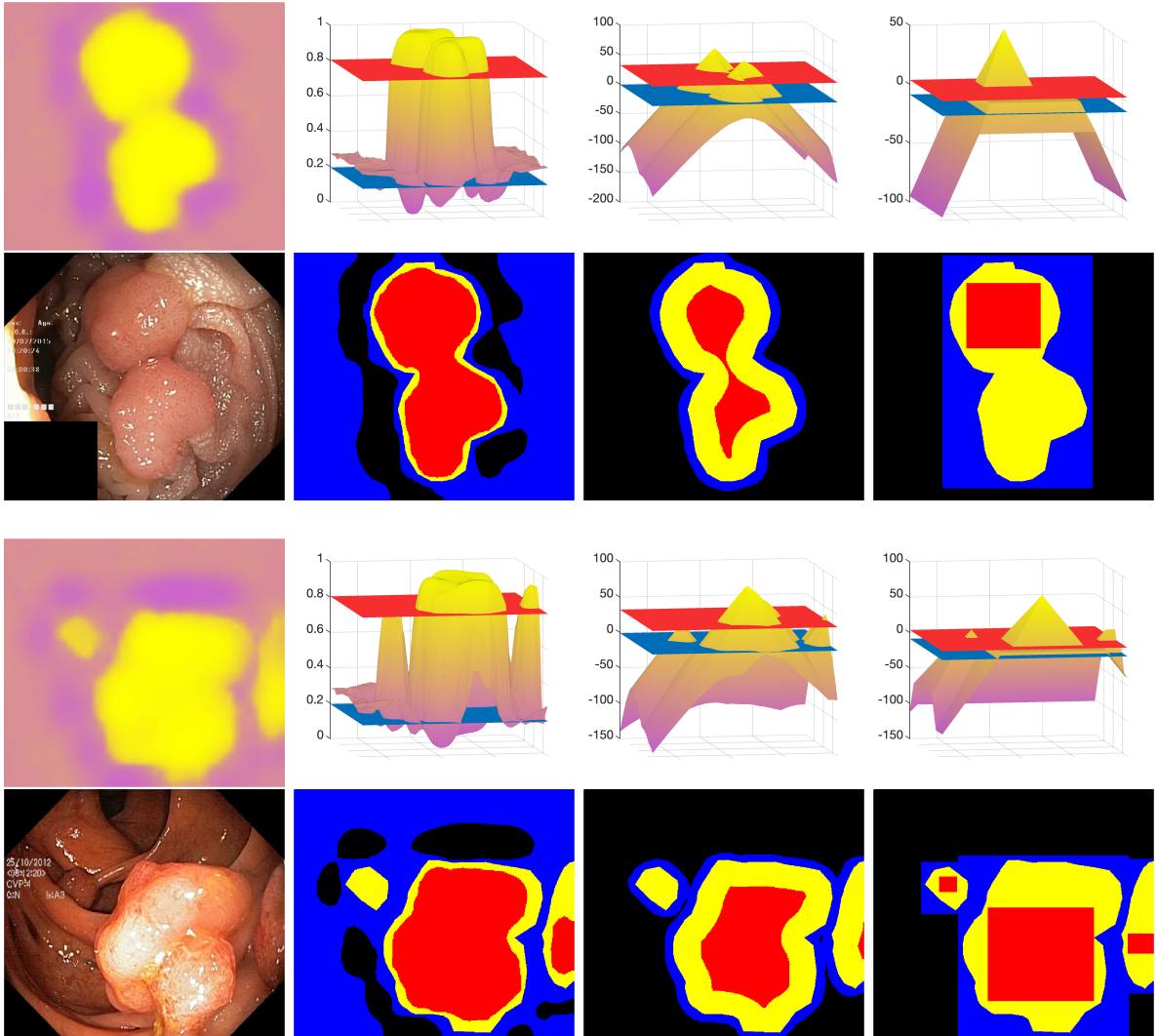


Figure 2: Illustrating the performance of the different score transformations on the learning dataset. We display 2 example tumors and present the results of each in 8 panels. These panels are as follows. Bottom left: the original image of the polyps tumor. Top Left: an intensity plot of the scores obtained from PraNet with purple/yellow indicating areas of lower/higher assigned probability. For the remaining panels, 3 different score transformations are shown which from left to right are the original scores, distance transformed scores $d_\rho(\hat{M}(X), v)$ and bounding box scores (obtained using the combined bounding box score b_M defined in Definition A.4). In each of the panels on the top row a surface plot of the transformed PraNet scores is shown, along with the conformal thresholds which are used to obtain the marginal 90% inner and outer confidence sets. These thresholds are illustrated via red and blue planes respectively and are obtained over the learning dataset. The panels on the bottom row of each example show the corresponding conformal confidence sets. Here the inner set is shown in red, plotted over the outer set which is shown in blue. The outer set contains the ground truth mask which contains the inner set in all examples. From these figures we see that the original scores provide tight inner confidence sets and the distance transformed scores instead provide tight outer confidence sets. The conclusion from the learning dataset is therefore that it makes sense to combine these two score transformations.

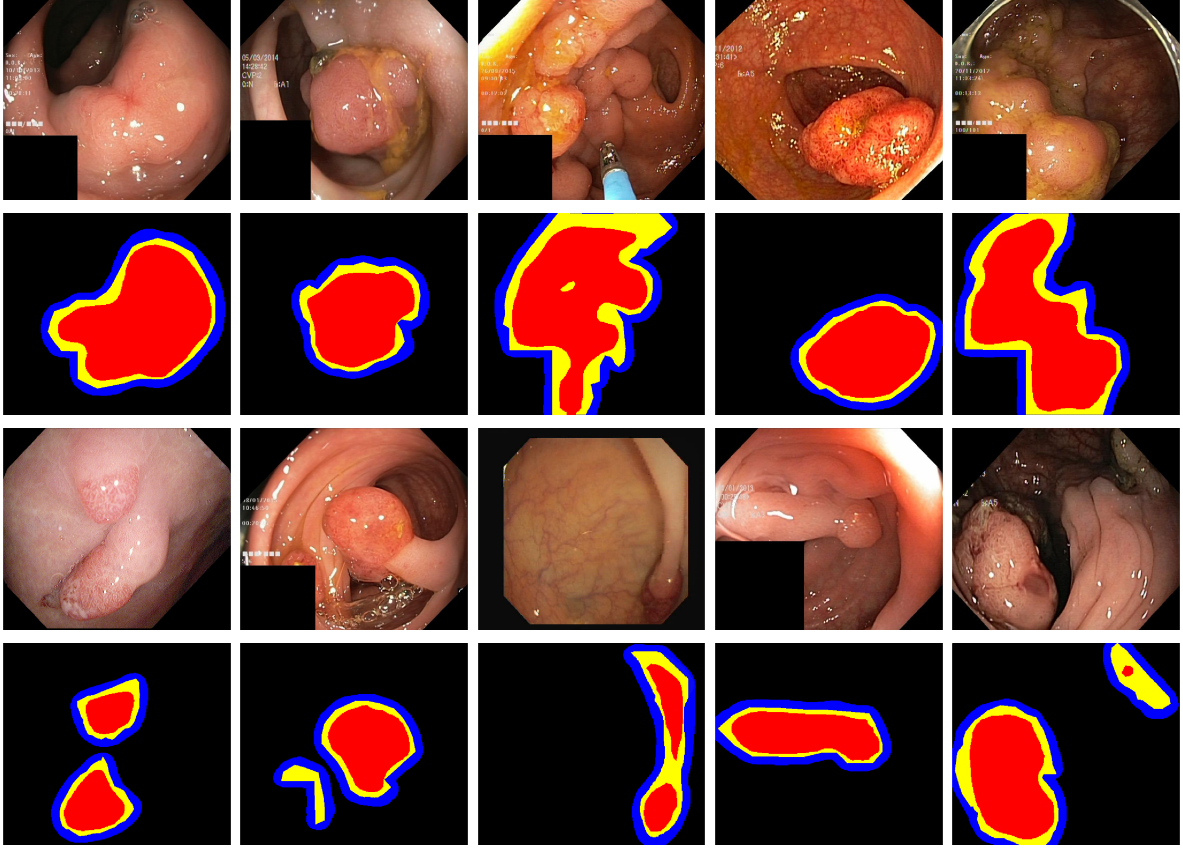


Figure 3: Conformal confidence sets for the polyps data. For each set of polyps images the top row shows the original endoscopic images with visible polyps and the second row presents the marginal 90% confidence sets, with ground truth masks shown in yellow. The inner sets and outer sets are shown in red and blue, obtained using the identity and distance transforms respectively. The figure shows the benefits of combining different score transformations for the inner and outer sets and illustrates the method’s effectiveness in accurately identifying polyp regions whilst providing informative spatial uncertainty bounds.

test dataset. We average over all 1000 validations and present the results in Figure 4. Histograms for the 90% coverage obtained over all validation runs are shown in Figure A15. From these results we can see that for all the approaches the coverage rate is controlled at or above the nominal level as desired. Using the bounding box scores results in slight over coverage at lower confidence levels. This is likely due to the discontinuities in the score functions b_I and b_O .

3.4 Comparing the efficiency of the bounds

In this section we compare the efficiency of the confidence sets based on the different score transformations. To do so we run 1000 validations in each dividing and calibrating as in Section 3.3. For each run we compute the ratio between the diameter of the inner set and the diameter of the ground truth mask and average this ratio over the 500 test images. In order to make a smooth curve we average this quantity over all 1000 runs. A similar calculation is performed for the outer set. The results are shown in Figure 5. They show that the inner confidence sets produced by using the original scores are the

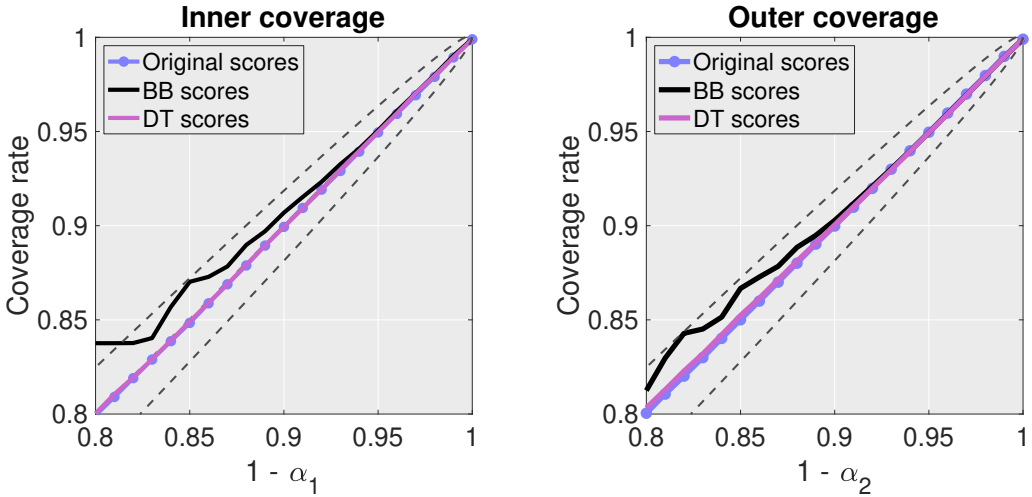


Figure 4: Coverage levels of the inner and outer sets averaged over 1000 validations for the original, distance transformed (DT) and bounding box (BB) scores.

most efficient. Instead, for the outer set, the distance transformed scores perform best. These results match the observations made on the learning dataset in Section 3.1 and the results found in Section 3.2.

We repeat this procedure instead targeting the proportion of the entire image which is under/over covered by the respective confidence sets. The results are shown in Figure 6 and can be interpreted similarly.

4 Discussion

In this work, we have developed conformal confidence sets which offer probabilistic guarantees for the output of a black box image segmentation model and provide tight bounds. Our work helps to address the lack of formal uncertainty quantification in the application of deep neural networks to medical imaging which has limited the reliability and adoption of these models in practice. The use of improved neural networks which can better separate the scores within and outside the ground truth masks would lead to more precise confidence sets and optimizing this is an important area of research. We have here established validity guarantees and additionally showed that these can be used to theoretically justify a modified version of the max-additive bounding box based method of Andéol et al. (2023).

The use of the distance transformed scores was crucial in providing tight outer confidence bounds as the original neural network is by itself unable to reliably determine where the tumors end with certainty. The distance transformation penalizes regions away from the predicted mask, allowing the tumors to be distinguished from the background. In other datasets and model settings, other transformations may be appropriate. As such we strongly recommend the use of a learning dataset in order to calibrate the transformations and maximize precision of the resulting confidence bounds.

The confidence sets we develop in this paper are related in spirit to work on uncertainty quantification for spatial excursion sets (Chen et al. (2017), Bowring et al. (2019), Mejia et al. (2020)). These approaches instead assume that multiple observations from a signal plus noise model are observed and perform inference on the underlying signal

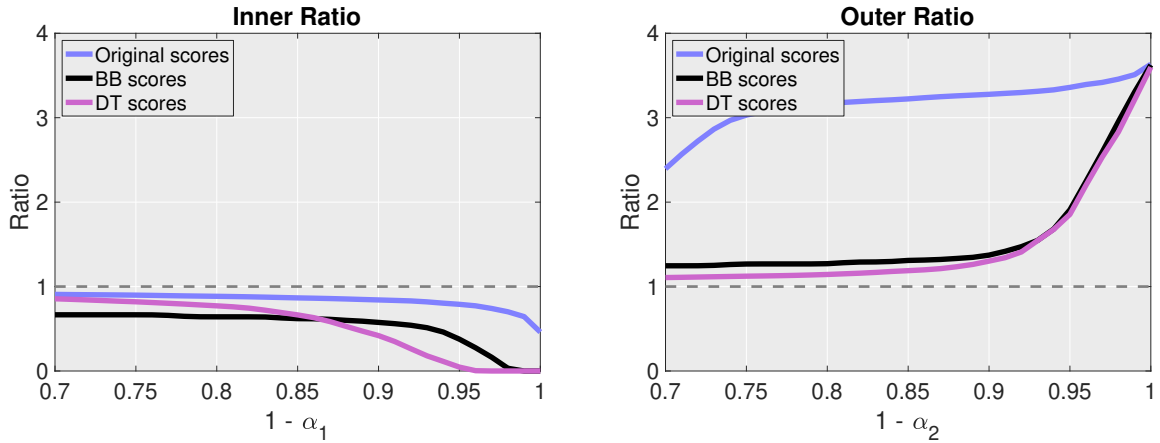


Figure 5: Measuring the efficiency of the bound using the ratio of the diameter of the coverage set to the diameter of the true tumor mask. The closer the ratio is to one the better. Higher coverage rates lead to a lower efficiency. The original scores provide the most efficient inner sets and the distance transformed scores provide the most efficient outer sets.

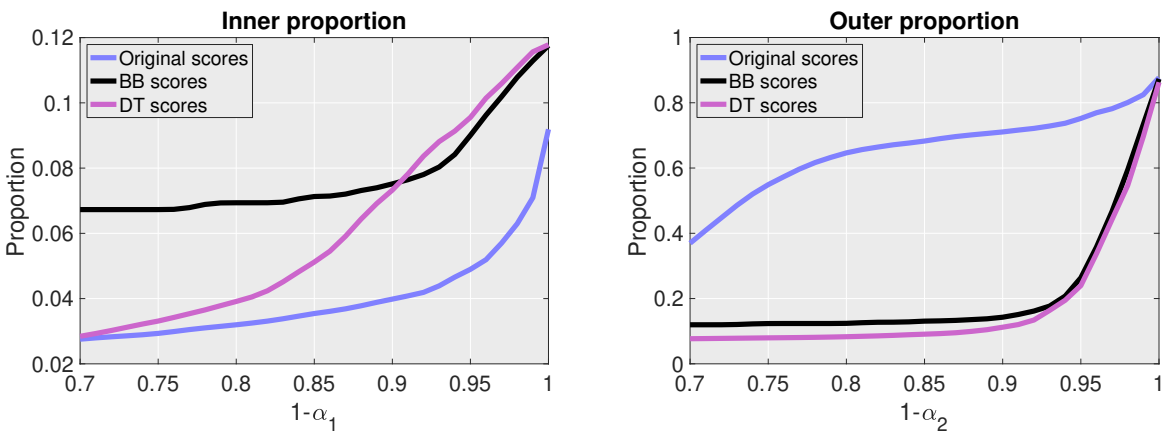


Figure 6: Measuring the proportion of the entire image which is under/over covered by the respective confidence sets. Left: proportion of the image which lies within the true mask but outside of the inner set. Right: proportion of the image which lies within the confidence set but outside of the true mask. For both a lower proportion corresponds to increased precision.

rather than prediction. Unlike conformal inference these approaches rely on central limit theorems or distributional assumptions in order to provide spatial confidence regions with asymptotic coverage guarantees.

Availability of code

Matlab code to implement the methods of this paper and a demo on a downsampled version of the data is available in the supplementary material. The code is very fast: calculating inner and outer thresholds (over the 1000 images in the calibration set) requires approximately 0.03 seconds on the downsampled data on a standard laptop (Apple M3 chip with 16 GB RAM) and 2.64 seconds for the original dataset.

Acknowledgements

I'm grateful to Habib Ganjgahi at the Big Data Institute at the University of Oxford for useful conversations on this topic. I'm also very grateful to Armin Schatzman at the University of San Diego, California for generous funding and support via NIH grant R01EB026859.

References

- Léo Andéol, Thomas Fel, Florence De Grancey, and Luca Mossina. Confident object detection via conformal prediction and conformal risk control: an application to railway signaling. In *Conformal and Probabilistic Prediction with Applications*, pages 36–55. PMLR, 2023.
- Anastasios N Angelopoulos and Stephen Bates. A gentle introduction to conformal prediction and distribution-free uncertainty quantification. *arXiv preprint arXiv:2107.07511*, 2021.
- Anastasios N Angelopoulos, Stephen Bates, Emmanuel J Candès, Michael I Jordan, and Lihua Lei. Learn then test: Calibrating predictive algorithms to achieve risk control. *arXiv preprint arXiv:2110.01052*, 2021.
- Anastasios N. Angelopoulos, Stephen Bates, Adam Fisch, Lihua Lei, and Tal Schuster. Conformal risk control. In *Proceedings of the International Conference on Learning Representations (ICLR)*, 2024.
- Stephen Bates, Anastasios Angelopoulos, Lihua Lei, Jitendra Malik, and Michael Jordan. Distribution-free, risk-controlling prediction sets. *Journal of the ACM (JACM)*, 68(6):1–34, 2021.
- Yoav Benjamini and Yosef Hochberg. Controlling the false discovery rate: a practical and powerful approach to multiple testing. *Journal of the Royal statistical society: series B (Methodological)*, 57(1):289–300, 1995.
- Jorge Bernal, Javier Sánchez, and Fernando Vilarino. Towards automatic polyp detection with a polyp appearance model. *Pattern Recognition*, 45(9):3166–3182, 2012.

Gilles Blanchard, Guillermo Durand, Ariane Marandon-Carlhian, and Romain Périer. Fdr control and fdp bounds for conformal link prediction. *arXiv preprint arXiv:2404.02542*, 2024.

Gunilla Borgefors. Distance transformations in digital images. *Computer vision, graphics, and image processing*, 34(3):344–371, 1986.

Hanna Borgli, Vajira Thambawita, Pia H Smedsrud, Steven Hicks, Debesh Jha, Sigrun L Eskeland, Kristin Ranheim Randel, Konstantin Pogorelov, Mathias Lux, Duc Tien Dang Nguyen, et al. Hyperkvasir, a comprehensive multi-class image and video dataset for gastrointestinal endoscopy. *Scientific data*, 7(1):283, 2020.

Alexander Bowring, Fabian Telschow, Armin Schwartzman, and Thomas E. Nichols. Spatial confidence sets for raw effect size images. *NeuroImage*, 203:116187, 2019.

Yen-Chi Chen, Christopher R Genovese, and Larry Wasserman. Density level sets: Asymptotics, inference, and visualization. *Journal of the American Statistical Association*, 112(520):1684–1696, 2017.

Florence de Grancey, Jean-Luc Adam, Lucian Alecu, Sébastien Gerchinovitz, Franck Mamalet, and David Vigouroux. Object detection with probabilistic guarantees. In *Fifth International Workshop on Artificial Intelligence Safety Engineering (WAISE 2022)*, 2022.

Deng-Ping Fan, Ge-Peng Ji, Tao Zhou, Geng Chen, Huazhu Fu, Jianbing Shen, and Ling Shao. Planet: Parallel reverse attention network for polyp segmentation. In *International conference on medical image computing and computer-assisted intervention*, pages 263–273. Springer, 2020.

Chuan Guo, Geoff Pleiss, Yu Sun, and Kilian Q Weinberger. On calibration of modern neural networks. In *International conference on machine learning*, pages 1321–1330. PMLR, 2017.

Chirag Gupta, Aleksandr Podkopaev, and Aaditya Ramdas. Distribution-free binary classification: prediction sets, confidence intervals and calibration. *Advances in Neural Information Processing Systems*, 33:3711–3723, 2020.

Seyed Ali Jalalifar, Hany Soliman, Arjun Sahgal, and Ali Sadeghi-Naini. Impact of tumour segmentation accuracy on efficacy of quantitative mri biomarkers of radiotherapy outcome in brain metastasis. *Cancers*, 14(20):5133, 2022.

Alain Jungo, Fabian Balsiger, and Mauricio Reyes. Analyzing the quality and challenges of uncertainty estimations for brain tumor segmentation. *Frontiers in neuroscience*, 14:282, 2020.

Carsten Maple. Geometric design and space planning using the marching squares and marching cube algorithms. In *2003 international conference on geometric modeling and graphics, 2003. Proceedings*, pages 90–95. IEEE, 2003.

Ariane Marandon. Conformal link prediction for false discovery rate control. *TEST*, pages 1–22, 2024.

Amanda F Mejia, Yu Yue, David Bolin, Finn Lindgren, and Martin A Lindquist. A bayesian general linear modeling approach to cortical surface fmri data analysis. *Journal of the American Statistical Association*, 115(530):501–520, 2020.

Luca Mossina, Joseba Dalmau, and Léo Andéol. Conformal semantic image segmentation: Post-hoc quantification of predictive uncertainty. In *Proceedings of the IEEE/CVF Conference on Computer Vision and Pattern Recognition*, pages 3574–3584, 2024.

Bruce Cyusa Mukama, Soundouss Messoudi, Sylvain Rousseau, and Sébastien Destercke. Copula-based conformal prediction for object detection: a more efficient approach. *Proceedings of Machine Learning Research*, 230:1–18, 2024.

Harris Papadopoulos, Kostas Proedrou, Volodya Vovk, and Alex Gammerman. Inductive confidence machines for regression. In *Machine learning: ECML 2002: 13th European conference on machine learning Helsinki, Finland, August 19–23, 2002 proceedings 13*, pages 345–356. Springer, 2002.

Edward F Patz, Paul Pinsky, Constantine Gatsonis, JoRean D Sicks, Barnett S Kramer, Martin C Tammemägi, Caroline Chiles, William C Black, Denise R Aberle, NLST Overdiagnosis Manuscript Writing Team, et al. Overdiagnosis in low-dose computed tomography screening for lung cancer. *JAMA internal medicine*, 174(2):269–274, 2014.

Konstantin Pogorelov, Kristin Ranheim Randel, Carsten Griwodz, Sigrun Losada Eskeland, Thomas de Lange, Dag Johansen, Concetto Spampinato, Duc-Tien Dang-Nguyen, Mathias Lux, Peter Thelin Schmidt, Michael Riegler, and Pål Halvorsen. Kvadir: A multi-class image dataset for computer aided gastrointestinal disease detection. In *Proceedings of the 8th ACM on Multimedia Systems Conference*, MMSys’17, pages 164–169, New York, NY, USA, 2017. ACM. ISBN 978-1-4503-5002-0. doi: 10.1145/3083187.3083212.

Glenn Shafer and Vladimir Vovk. A tutorial on conformal prediction. *Journal of Machine Learning Research*, 9(3), 2008.

Juan Silva, Aymeric Histace, Olivier Romain, Xavier Dray, and Bertrand Granado. Toward embedded detection of polyps in wce images for early diagnosis of colorectal cancer. *International journal of computer assisted radiology and surgery*, 9:283–293, 2014.

Sophia Sun and Rose Yu. Copula conformal prediction for multi-step time series forecasting. In *International Conference on Learning Representations (ICLR)*, 2024.

Ryan J Tibshirani, Rina Foygel Barber, Emmanuel Candes, and Aaditya Ramdas. Conformal prediction under covariate shift. *Advances in neural information processing systems*, 32, 2019.

Eric J Topol. High-performance medicine: the convergence of human and artificial intelligence. *Nature medicine*, 25(1):44–56, 2019.

Vladimir Vovk, Alexander Gammerman, and Glenn Shafer. *Algorithmic learning in a random world*, volume 29. Springer, 2005.

Håkan Wieslander, Philip J Harrison, Gabriel Skogberg, Sonya Jackson, Markus Fridén, Johan Karlsson, Ola Spjuth, and Carolina Wählby. Deep learning with conformal prediction for hierarchical analysis of large-scale whole-slide tissue images. *IEEE journal of biomedical and health informatics*, 25(2):371–380, 2020.

Keith J. Worsley, Alan C Evans, Sean Marrett, and P Neelin. A three-dimensional statistical analysis for CBF activation studies in human brain. *JCBFM*, 1992.

A Appendix

A.1 Obtaining conformal confidence sets with increasing combination functions

As discussed in Remark 2.3 the results of Sections 2.2 and 2.3 can be generalized to a wider class of combination functions.

Definition A.1. We define a suitable combination function to be a function $C : \mathcal{P}(\mathcal{V}) \times \mathcal{X} \rightarrow \mathbb{R}$ which is increasing in the sense that for all sets $\mathcal{A} \subseteq \mathcal{V}$ and each $v \in \mathcal{A}$, $C(v, X) \leq C(\mathcal{A}, X)$ for all $X \in \mathcal{X}$.

The maximum is a suitable combination function since $X(v) = \max_{v \in \{v\}} X(v) \leq \max_{v \in \mathcal{A}} X(v)$. As such this framework directly generalizes the results of the main text.

We can construct generalized marginal confidence sets as follows.

Theorem A.2. (*Marginal inner set*) Under Assumptions 1 and 2, given $\alpha_1 \in (0, 1)$, define

$$\lambda_I(\alpha_1) = \inf \left\{ \lambda : \frac{1}{n} \sum_{i=1}^n \mathbb{1}[C(\{v \in \mathcal{V} : Y_i(v) = 1\}, f_I(s(X_i))) \leq \lambda] \geq \frac{\lceil (1 - \alpha_1)(n + 1) \rceil}{n} \right\},$$

for a suitable combination function C , and define $I(X) = \{v \in \mathcal{V} : C(v, f_I(s(X))) > \lambda_I(\alpha_1)\}$. Then,

$$\mathbb{P}(I(X_{n+1}) \subseteq \{v \in \mathcal{V} : Y_{n+1}(v) = 1\}) \geq 1 - \alpha_1. \quad (7)$$

The proof follows that of Theorem 2.1. The key observation is that for any suitable combination function C , given $\lambda \in \mathbb{R}$, $\mathcal{A} \subseteq \mathcal{V}$ and $X \in \mathcal{X}$, $C(\mathcal{A}, X) \leq \lambda$ implies that $C(v, X) \leq \lambda$. This is the relevant property of the maximum which we used for the results in the main text. For the outer set we similarly have the following.

Theorem A.3. (*Marginal outer set*) Under Assumptions 1 and 2, given $\alpha_2 \in (0, 1)$, define

$$\lambda_O(\alpha_2) = \inf \left\{ \lambda : \frac{1}{n} \sum_{i=1}^n \mathbb{1}[C(\{v \in \mathcal{V} : Y_i(v) = 0\}, -f_O(s(X_i))) \leq \lambda] \geq \frac{\lceil (1 - \alpha_2)(n + 1) \rceil}{n} \right\}.$$

for a suitable combination function C , and let $O(X) = \{v \in \mathcal{V} : C(v, -f_O(s(X))) \leq \lambda_O(\alpha_2)\}$. Then,

$$\mathbb{P}(\{v \in \mathcal{V} : Y_{n+1}(v) = 1\} \subseteq O(X_{n+1})) \geq 1 - \alpha_2. \quad (8)$$

Joint results can be analogously obtained.

A.2 Obtaining confidence sets from risk control

We can alternatively establish Theorems 2.1 and A.2 using an argument from risk control (Angelopoulos et al., 2024). In particular, given an image pair (X, Y) and $\lambda \in \mathbb{R}$, let

$$I_\lambda(X) = \{v \in \mathcal{V} : f_I(s(X), v) > \lambda\}.$$

Define a loss function, $L : \mathcal{P}(\mathcal{V}) \times \mathcal{Y} \rightarrow \mathbb{R}$ which sends (X, Y) to

$$L(I_\lambda(X), Y) = \mathbb{1}[I_\lambda(X) \not\subseteq \{v \in \mathcal{V} : Y(v) = 1\}].$$

For $i = 1, \dots, n+1$, let $L_i(\lambda) = L(I_\lambda(X_i), Y_i)$. Arguing as in the proof of Theorem 2.1 it follows that $L_i(\lambda) = 1[\tau_i > \lambda]$. Then applying Theorem 1 of Angelopoulos et al. (2024) it follows that

$$\mathbb{E} [L_{n+1}(\hat{\lambda})] \leq \alpha_1,$$

where $\hat{\lambda} = \inf \left\{ \lambda : \frac{1}{n} \sum_{i=1}^n L_i(\lambda) \leq \alpha_1 - \frac{1-\alpha_1}{n} \right\}$. Arguing as in Appendix A of (Angelopoulos et al., 2024) it follows that

$$\hat{\lambda} = \inf \left\{ \lambda : \frac{1}{n} \sum_{i=1}^n 1[\tau_i \leq \lambda] \geq \frac{(1-\alpha_1)(n+1)}{n} \right\} = \lambda_I(\alpha_1),$$

and so $I(X) = I_{\hat{\lambda}}(X)$. As such

$$\mathbb{P}(I(X_{n+1}) \subseteq \{v \in \mathcal{V} : Y_{n+1}(v) = 1\}) = 1 - \mathbb{E}[L_{n+1}(\hat{\lambda})] \geq 1 - \alpha_1, \quad (9)$$

and we recover the desired result. Arguing similarly it is possible to establish a proof of Theorem 2.2.

A.3 Providing theory for deriving confidence sets from bounding boxes

We can use our results in order to provide valid inference for bounding boxes. In what follows we adapt the approach of Andéol et al. (2023) in order to ensure validity. In particular given $Z \in \mathcal{Y}$, let $B_{I,\max}(Z)$ be the largest box which can be contained within the set $\{v \in \mathcal{V} : Z(v) = 1\}$ and let $B_{O,\min}(Z)$ be the smallest box which contains the set $\{v \in \mathcal{V} : Z(v) = 1\}$. Given $Y \in \mathcal{Y}$, let $cc(Y) \subseteq \mathcal{P}(\mathcal{V})$ denote the set of connected components of the set $\{v \in \mathcal{V} : Y(v) = 1\}$ for a given connectivity criterion (which we take to be 4 in our examples), and note that these components can themselves be identified as elements of \mathcal{Y} . Define

$$B_I(Y) = \cup_{c \in cc(Y)} B_{I,\max}(c) \text{ and } B_O(Y) = \cup_{c \in cc(Y)} B_{O,\min}(c)$$

to be the unions of the largest inner and smallest outer boxes of the connected components of the image Y , respectively. Then define

$$\hat{B}_I(s(X)) = \cup_{c \in cc(\hat{M}(X))} B_{I,\max}(c) \text{ and } \hat{B}_O(s(X)) = \cup_{c \in cc(\hat{M}(X))} B_{O,\min}(c)$$

to be the unions of the largest inner and smallest outer boxes of the connected components of the predicted mask $\hat{M}(X)$, respectively. Note that this is well-defined as $\hat{M}(X)$ is a function of $s(X)$.

For the remainder of this section we shall assume that $\mathcal{V} \subset \mathbb{R}^2$, this is not strictly necessary but will help to simplify notation. Given $u, v \in \mathcal{V}$, write $u = (u_1, u_2)$ and $v = (v_1, v_2)$ and let $\rho(u, v) = \max(|u_1 - v_1|, |u_2 - v_2|)$ be the chessboard metric.

Definition A.4. (Bounding box scores) For each $X \in \mathcal{X}$ and $v \in \mathcal{V}$, let

$$b_I(s(X), v) = d_\rho(\hat{B}_I(s(X)), v) \text{ and } b_O(s(X), v) = d_\rho(\hat{B}_O(s(X)), v)$$

be the distance transformed scores based on the chessboard distance to the predicted inner and outer box collections $\hat{B}_I(s(X))$ and $\hat{B}_O(s(X))$, respectively. We also define a combination of these b_M , primarily for the purposes of plotting in Figure 2, as follows. Let $b_M(s(X), v) = b_O(s(X), v)$ for each $v \notin \hat{B}_O(s(X))$ and let $b_M(s(X), v) = \max(b_I(s(X), v), 0)$ for $v \in \hat{B}_O(s(X))$. We shall write $b_I(s(X)) \in \mathcal{X}$ to denote the image which has $b_I(s(X))(v) = b_I(s(X), v)$ and similarly for $b_O(s(X))$ and $b_M(s(X))$.

Now consider the sequences of image pairs $(X_i, B_i^I)_{i=1}^n$ and $(X_i, B_i^O)_{i=1}^n$. These both satisfy exchangeability and so, applying Theorems A.2 and A.3, we obtain the following bounding box validity results.

Corollary A.5. (*Marginal inner bounding boxes*) Suppose Assumption 1 holds and that $(X_i, Y_i)_{i=1}^{n+1}$ is independent of the functions s and b_I . Given $\alpha_1 \in (0, 1)$, define

$$\lambda_I(\alpha_1) = \inf \left\{ \lambda : \frac{1}{n} \sum_{i=1}^n 1 [C(B_i^I, b_I(s(X_i))) \leq \lambda] \geq \frac{\lceil (1 - \alpha_1)(n + 1) \rceil}{n} \right\}, \quad (10)$$

for a suitable combination function C , and define $I(X) = \{v \in \mathcal{V} : C(v, b_I(s(X))) > \lambda_I(\alpha_1)\}$. Then,

$$\mathbb{P}(I(X_{n+1}) \subseteq B_{n+1}^I \subseteq \{v \in \mathcal{V} : Y_{n+1}(v) = 1\}) \geq 1 - \alpha_1.$$

Corollary A.6. (*Marginal outer bounding boxes*) Suppose Assumption 1 holds and that $(X_i, Y_i)_{i=1}^{n+1}$ is independent of the functions s and b_O . Given $\alpha_2 \in (0, 1)$, define

$$\lambda_O(\alpha_2) = \inf \left\{ \lambda : \frac{1}{n} \sum_{i=1}^n 1 [C(B_i^O, -b_O(s(X_i))) \leq \lambda] \geq \frac{\lceil (1 - \alpha_2)(n + 1) \rceil}{n} \right\}. \quad (11)$$

for a suitable combination function C , and let $O(X) = \{v \in \mathcal{V} : C(v, -b_O(s(X))) \leq \lambda_O(\alpha_2)\}$. Then,

$$\mathbb{P}(\{v \in \mathcal{V} : Y_{n+1}(v) = 1\} \subseteq B_{n+1}^O \subseteq O(X_{n+1})) \geq 1 - \alpha_2.$$

Joint results can be obtained in a similar manner to those in Section 2.3.

A.4 Additional examples from the learning dataset

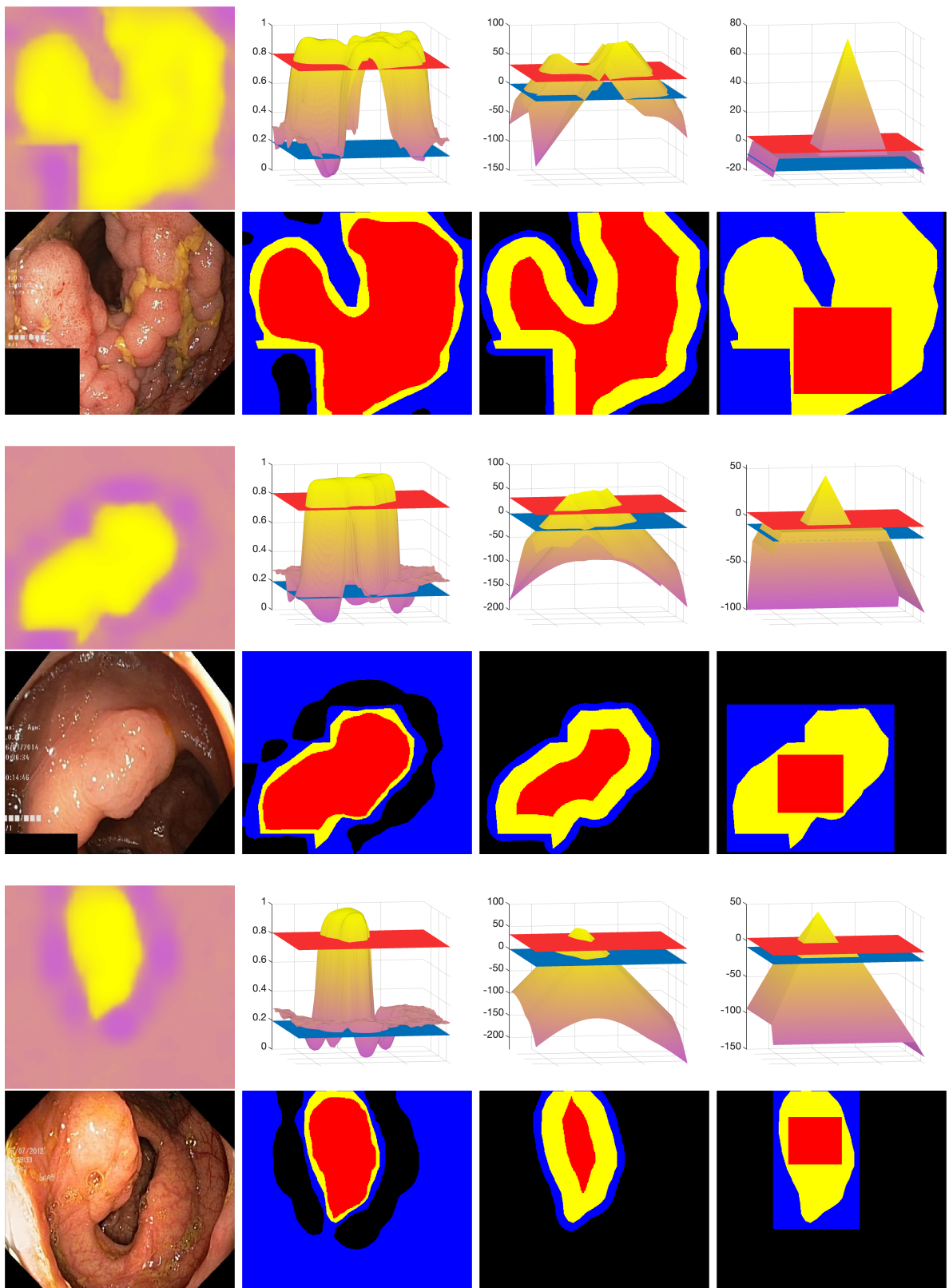


Figure A7: Additional examples from the learning dataset. The layout of these figures is the same as for Figure 2.

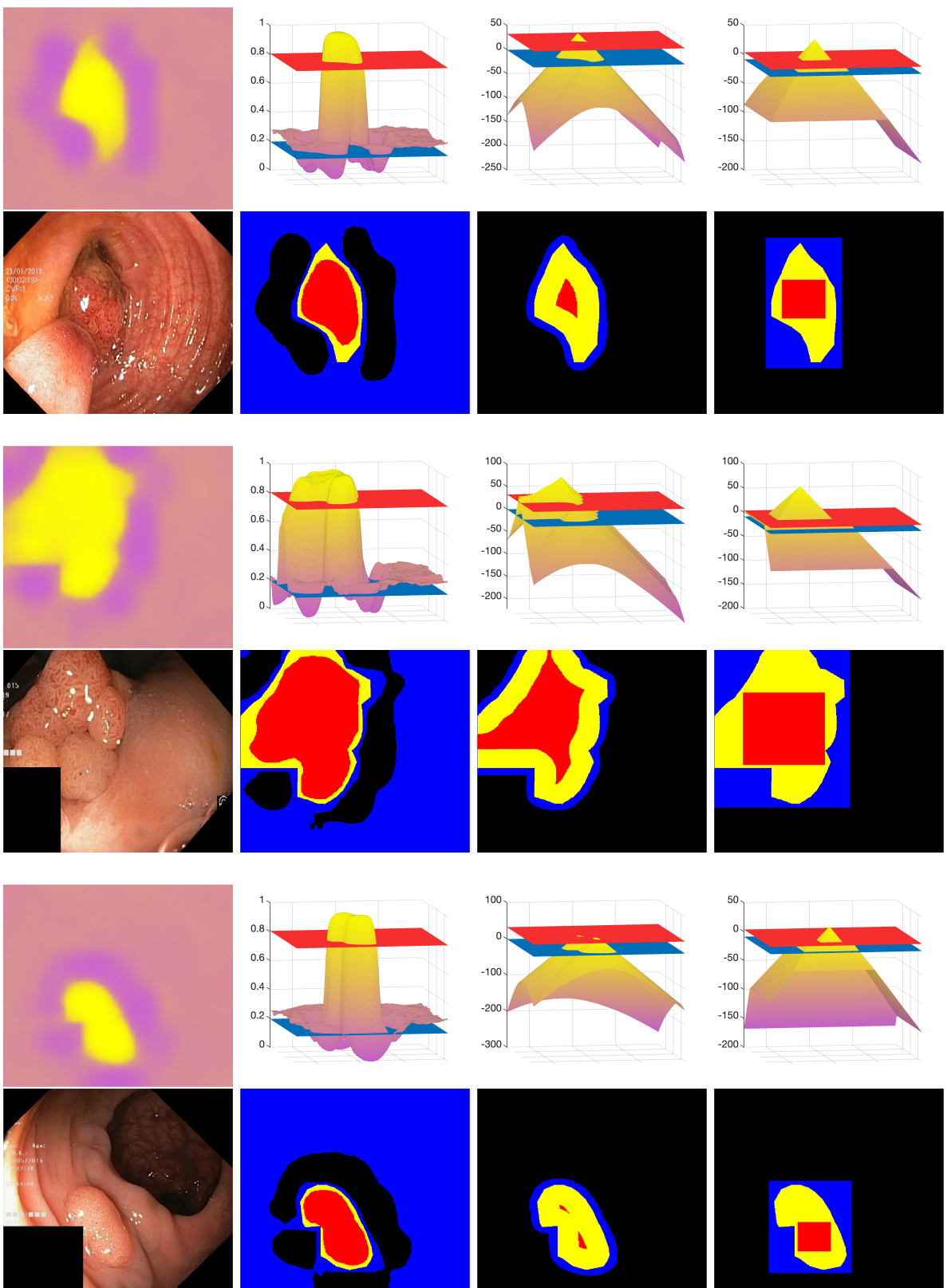


Figure A8: Futher examples from the learning dataset. The layout of these figures is the same as for Figure 2.

A.5 Validation figures for the original and bounding box scores

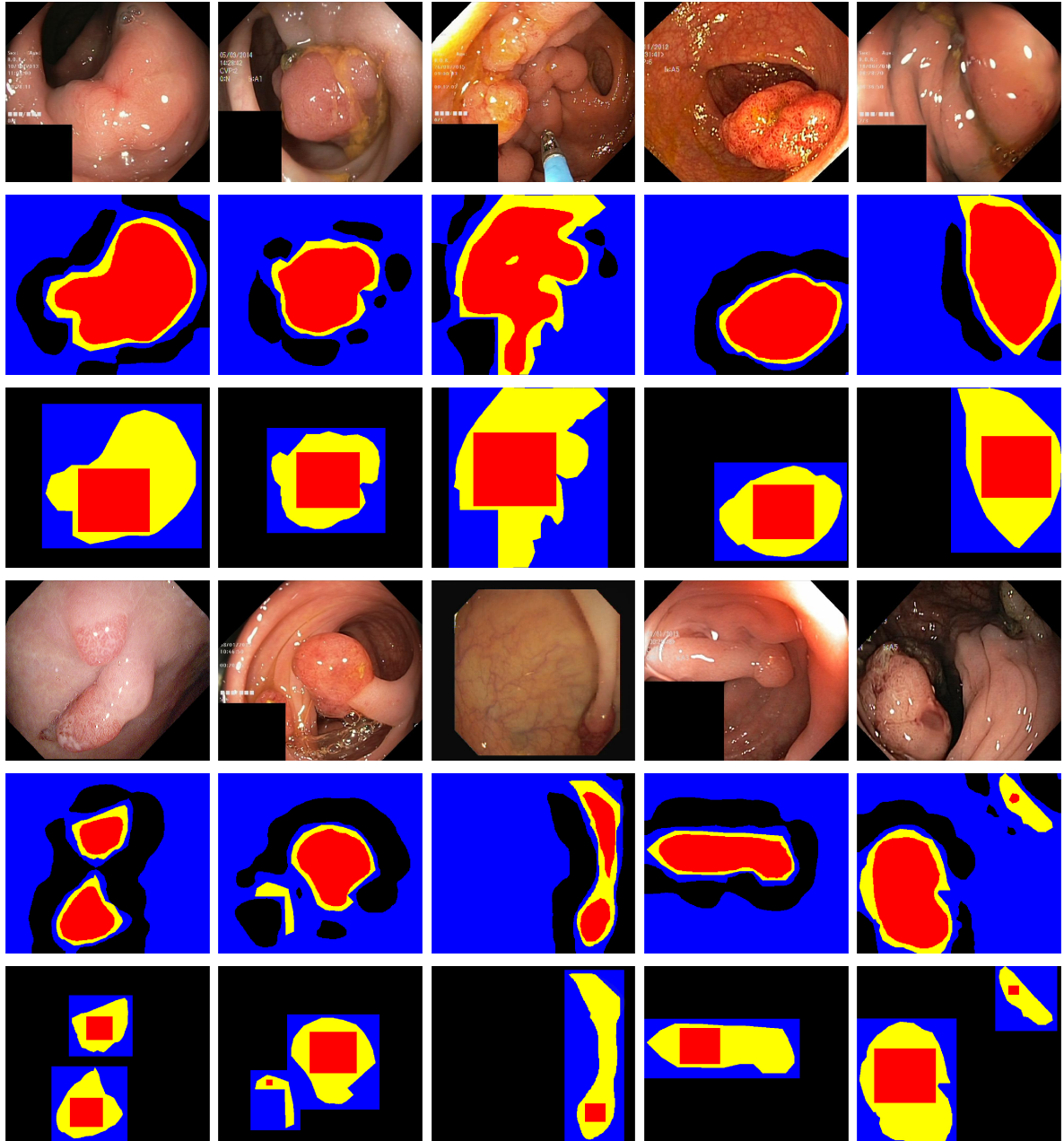


Figure A9: Conformal confidence sets for the polyps data examples from Figure 3 for alternative scores. In each set of panels the confidence obtained from using the original scores are shown in the middle row and those obtained from the bounding box scores are shown in the bottom row. As observed on the learning dataset the outer sets obtained when using the original scores are very large and uninformative.

A.6 Additional validation figures

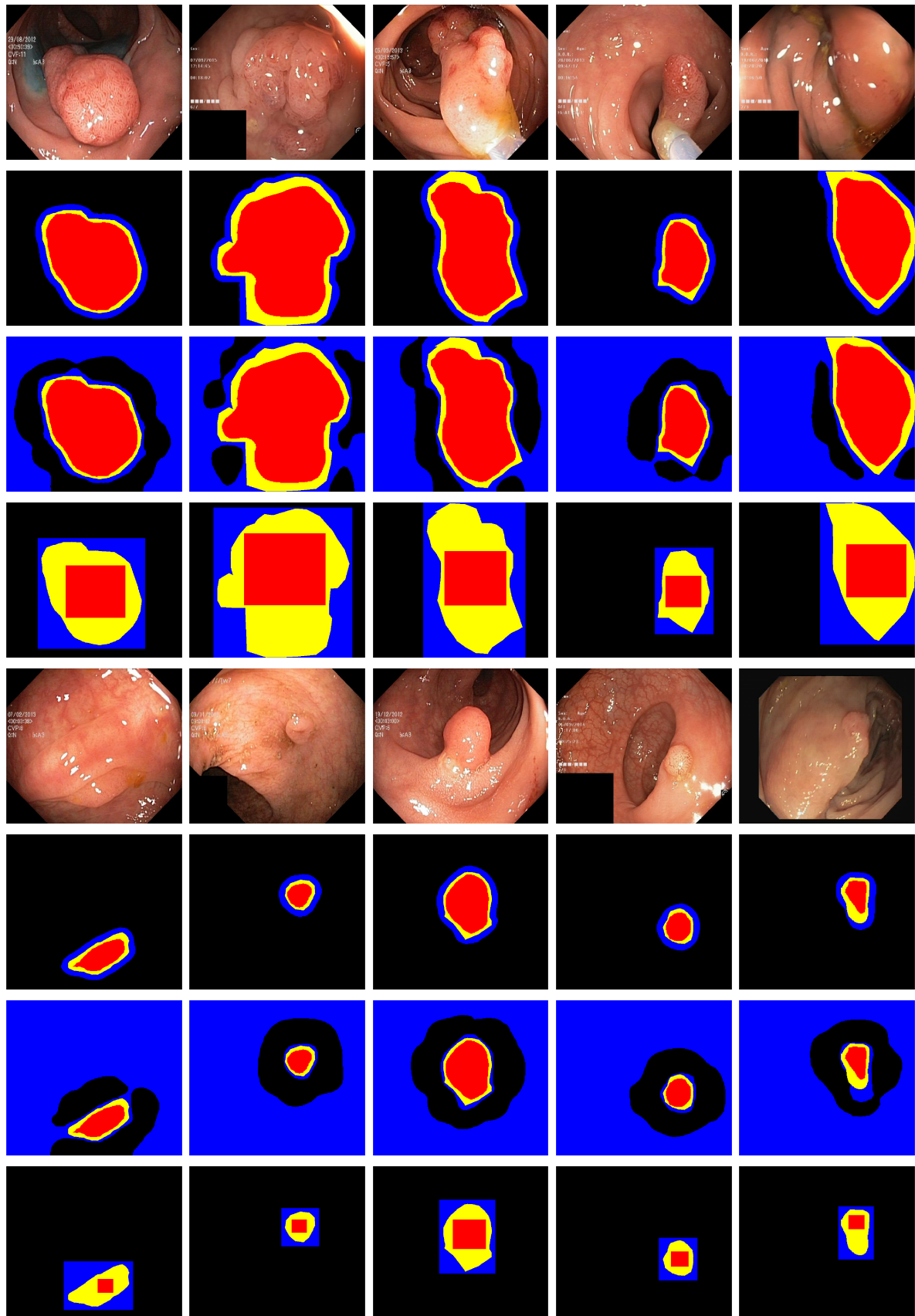


Figure A10: Additional validation examples. In each example, after the original images, the rows are (from top to bottom) the combination of the original and distance transformed scores, then the original scores and finally the bounding box scores.

A.7 Confidence sets for the bounding boxes

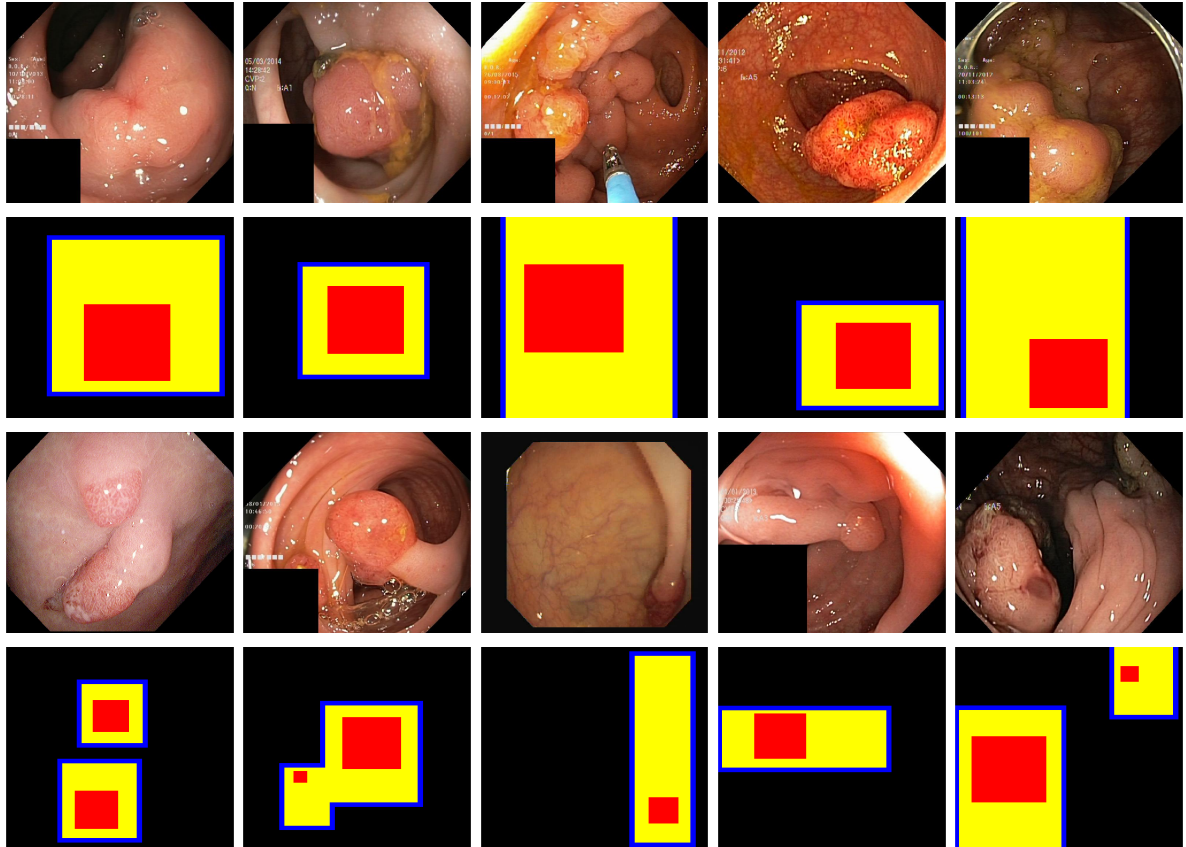


Figure A11: Conformal confidence sets for the boundary boxes themselves using the approach introduced in Section A.3. The ground truth outer bounding boxes are shown in yellow.

A.8 Joint 90% confidence regions

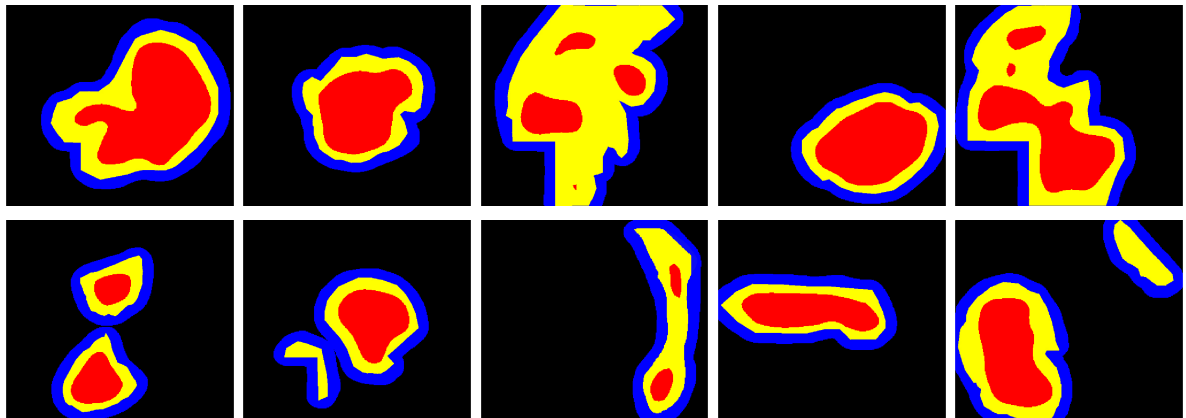


Figure A12: Joint 90% conformal confidence sets obtained using Corollary 2.5, with $\alpha_1 = 0.02$ and $\alpha_2 = 0.08$, for the polyps images in Figure 3.

A.9 Marginal 80 % Confidence regions

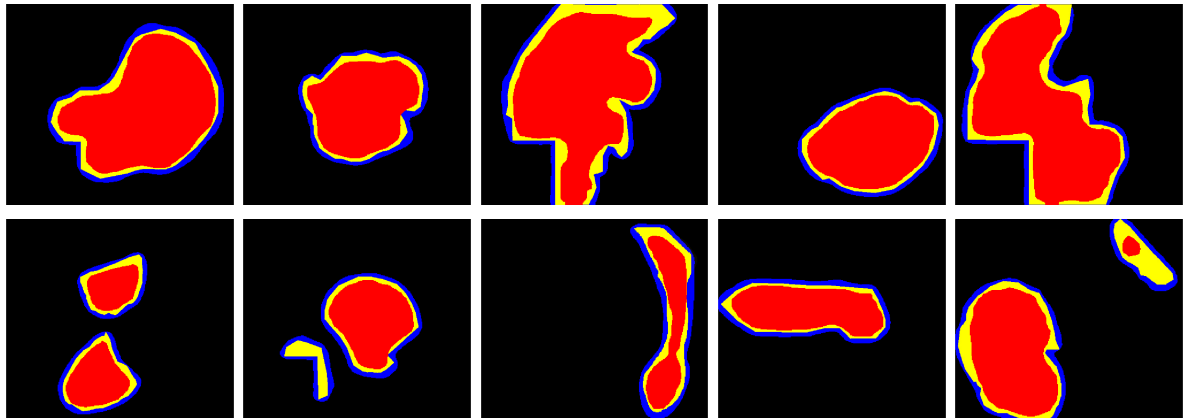


Figure A13: Marginal 80% conformal confidence sets obtained for the polyps images in Figure 3.

A.10 Marginal 95 % Confidence regions

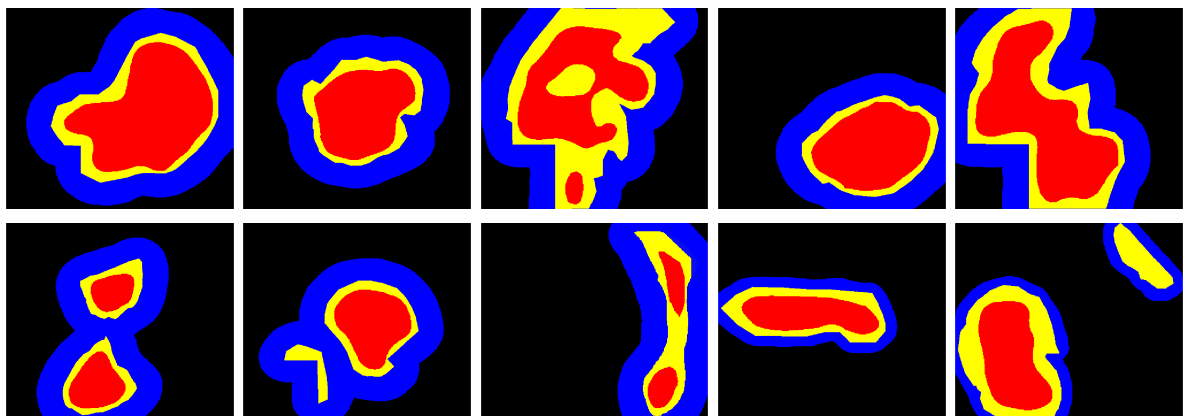


Figure A14: Marginal 95% conformal confidence sets obtained using for the polyps images in Figure 3. These sets are also joint 90% confidence sets with equally weighted $\alpha_1 = \alpha_2 = 0.05$. The influence of the weighting scheme can therefore examined by comparing to Figure A12.

A.11 Histograms of the coverage

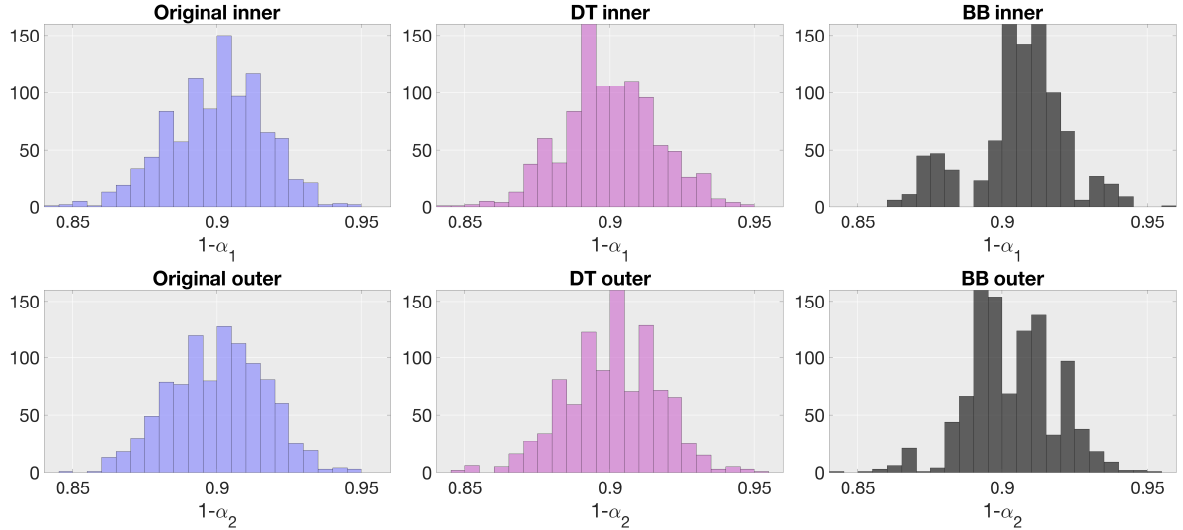


Figure A15: Histograms of the coverage rates obtained across each of the validation resamples for 90% inner and outer marginal confidence sets. We plot the results for the original scores, distance transformed scores (DT) and boundary box scores (BB) from left to right. The bounding box scores are discontinuous which is the cause of the discreteness of the rightmost histograms.